A Simplified Method for the Histochemical Detection of Iron in Paraffin Sections: Intracellular Iron Deposits in Central Nervous System Tissue

Steven M. LeVine[1] [iD], Hao Zhu[2,3,4] and Sarah E. Tague[5] [iD]

Abstract

Although all cells contain iron, most histochemical methods fail to reveal the presence of iron within many cells of the central nervous system (CNS), particularly neurons. Previously, a sensitive method was developed that limited the extraction of iron in paraffin sections, and this method revealed staining within neurons. However, the staining was often too robust making it difficult to discern discrete intracellular structures. In 1970, a study incorporated acetone in an iron histochemical procedure to facilitate the demarcation of staining features. In the present study, both acetone and limits to iron extraction were included in a simplified staining procedure. This procedure was applied to paraffin sections of CNS tissue from CISD2 deficient and littermate control mice. Discrete nuclear and cytoplasmic staining features were detected in all mice. Although widely present in neurons, punctate cytoplasmic staining was particularly prominent in large neurons within the hindbrain. Evaluation of extended depth of focus images, from serial focal planes, revealed numerous stained cytoplasmic structures. Additionally, the simplified staining procedure was applied to paraffin sections from Alzheimer's disease and control cases. Despite suboptimal processing conditions compared to mouse tissue, discrete staining of cytoplasmic structures was revealed in some neurons, although many other neurons had nondescript staining features. In addition, initial findings revealed iron deposited within some vessels from patients with Alzheimer's disease. In summary, since paraffin sections are commonly used for histological preparations, this simplified histochemical procedure could facilitate the study of iron in various CNS conditions by revealing staining details often missed by other procedures.

Keywords

Alzheimer's disease, amyloid, CISD2, histochemistry, iron, mitochondria, neuron, paraffin, vessel

Received September 9, 2020; Revised October 30, 2020; Accepted for publication November 19, 2020

Staining methods employed for microscopic analysis commonly utilize paraffin sections. However, the processing steps that are used for paraffin sections can extract compounds that are normally present within a tissue. Thus, a stain can underrepresent the in situ concentration of a compound. For instance, despite the presence of iron within all cells, standard histochemical staining of iron, with or without diaminobenzidine (DAB) enhancement, resulted in most cells being unstained within central nervous (CNS) tissue (Craelius et al., 1982; Walton and Kaufmann, 1984; Adams, 1988; Gerber and Connor, 1989; Connor et al., 1990; Castelnau et al., 1998; Moos and Morgan, 2002; Dong et al., 2015; Bulk et al., 2018a).

[1]Department of Molecular and Integrative Physiology, University of Kansas Medical Center, Kansas City, Kansas, United States
[2]Department of Clinical Laboratory Sciences, University of Kansas Medical Center, Kansas City, Kansas, United States
[3]Neuroscience Graduate Program, University of Kansas Medical Center, Kansas City, Kansas, United States
[4]Department of Biochemistry and Molecular Biology, University of Kansas Medical Center, Kansas City, Kansas, United States
[5]Kansas Intellectual and Developmental Disabilities Research Center, University of Kansas Medical Center, Kansas City, Kansas, United States

Corresponding Author:
Steven LeVine, Department of Molecular and Integrative Physiology, Mail Stop 3043, University of Kansas Medical Center, Kansas City, KS 66160, United States.
Email: slevine@kumc.edu

The absence of staining is due, in large part, to the extraction of iron when paraffin sections undergo deparaffinization followed by rehydration through alcohols to water (Sands et al., 2016).

When a modified, DAB-enhanced histochemical procedure was performed directly on paraffin sections, without paraffin extraction and rehydration steps, the detection of iron was widespread (Sands et al., 2016). However, this can lead to staining that is almost too robust with areas of extraneous staining. To eliminate this excess staining, paraffin sections were deparffinized, air dried, and then directly stained without rehydration through alcohols (Sands et al., 2016). This resulted in the removal of extraneous staining while still enabling robust labeling of cells within the CNS.

Although punctate labeling was often detected within cells with this modified method (Sands et al., 2016), robust nuclear or cytoplasmic staining frequently obfuscated the demarcation of individual intracellular structures. Thus, it was reasoned that the elimination of some steps designed to amplify the modified histochemical stain could improve the resolution of subcellular structures. In addition, a study from 1970 observed that discrete staining of structures could be enhanced by including acetone in the staining solution (Hirose et al., 1970). Acetone was thought to decrease the diffusion of the Prussian blue reaction product leading to greater staining definition (Hirose et al., 1970). Thus, we hypothesized that greater resolution of intracellular structures in paraffin sections would be obtained by a simplified method that limited iron extraction followed by incorporating acetone in the staining solution. The enhanced resolution obtained by such a method would enable the careful study of the spatial distribution and morphological features of stained intracellular structures.

Materials and Methods

Animals and Tissue Processing

The CISD2 mouse line was generated from ES cells carrying an engineered allele (exon1-2 deletion) and provided as a gift by Dr. Fumihiko Urano at Washington University School of Medicine. Male CISD2-null (KO) and wild-type (WT: heterozygous or homozygous for wild type allele) mice were generated from crosses between heterozygous breeders and maintained in a pathogen-free facility at 24°C under standard 12-hr light/12-hr dark cycle with unlimited access to water and a standard chow. In order to maximize the utilization of animals, the staining method described below was applied to animals that had completed another experiment that involved administering water containing deferiprone (1 mg/ml, Sigma) between weaning and 15 weeks of age. In preparation for the present study, animals were then given chow and water only (wash out) for two weeks prior to sacrifice, which should have acted to reverse any changes due to the drug especially given its short half-life (Kontoghiorghes et al., 1990). All animal experiments were performed in accordance with the National Institutes of Health Guide for the Care and Use of Laboratory Animals and approved by the University of Kansas Medical Center Institutional Animal Care and Use Committee.

Mice were anesthetized with isoflurane and perfused with cold fixative (4% paraformaldehyde with 0.1% sucrose diluted in Hank's balanced salt solution) followed by immersion fixation at 4°C (~3.5 days) and processing for paraffin embedding: upgraded ethanols; xylene substitute; and Paraplast X-TRA (total time ~13 h). Sagittal paraffin sections, 6 μm thick, of the cerebrum and hindbrain were floated onto glass slides, which were placed in an oven (38°C for ~3 days) and then stored at room temperature.

Human CNS Tissue

Deidentified human paraffin sections, 6 μm thick (baked at 65°C for 90 min), of the entorhinal cortex/hippocampus, from pathologically characterized cases (two subjects without Alzheimer's disease changes and two cases with high levels of neuropathological changes of Alzheimer disease) were provided by the University of Kansas Alzheimer's Disease Center. The post-mortem interval was 13 to 21 hr. The cases of Alzheimer's disease also displayed amyloid angiopathy and atherosclerosis or arteriolosclerosis.

Staining Procedure

Sections were deparaffinized with SafeClear (Fisher Scientific, catalog number 23314629) (2×3 min), excess SafeClear tapped off, and then stained with 50% acetone/1% potassium ferrocyanide trihydrate (Millipore Sigma, catalog number P3289-100G)/0.05 N HCl (final concentrations) for 1 hr; followed by washes in H_2O; 40 mg 3,3′-diaminobenzidine tetrahydrochloride (DAB) (Millipore Sigma, catalog number D5905) in 160 ml Tris buffered saline (Millipore Sigma, catalog number 94158-10TAB) with 640 μl 30% hydrogen peroxide for 30 min; H_2O; upgraded alcohols; SafeClear; permanent mounting media.

Instead of the 70–80% acetone used by Hirose et al. (1970), we observed that a 50% acetone concentration gave a suitable balance between allowing enough solubility of potassium ferrocyanide, the iron histochemical reagent, and the ability to achieve discrete staining. Furthermore, this concentration of acetone facilitated the wetting of the tissue section following the SafeClear step. Control slides were stained with 50% acetone/0.05 N HCl in place of the 50% acetone/1% potassium ferrocyanide trihydrate/0.05 N HCl solution.

Microscopy and Image Analysis

A Nikon 80i microscope with a DS-Fi3 camera was used to capture images using objectives 1× Plan UW (NA [numerical aperture] 0.04), 4× Plan Fluor (NA 0.13), 10× Plan Fluor (NA 0.30), 20× Plan Fluor (NA 0.5) and 40× Plan Fluor (NA 0.75). Since DAB-staining was found to absorb blue light, sometimes the white balance was adjusted towards a blue background, to reduce under-saturated pixels in the blue channel, improve radiometric resolution, and reveal staining details. For presentation of images, Photoshop CC 2017 was used to make adjustments to the color balance, contrast and/or brightness uniformly across the entire image area.

For mouse sections, Z-Stacked microscopy images were acquired using a Nikon Digital Sight DS-Fi2 color camera on a Nikon TE2000E microscope with a 60× Plan Apo oil objective (NA 1.4) and NIS-Elements Advanced Research software. The Z-stacks were acquired at 0.25 µm intervals through the top and bottom of cells of interest. Focused 2D projection images were created from Z-stack images using Nikon Elements AR Extended Depth of Focus (EDF). Adjustments to image levels were applied uniformly across the entire area of the EDF or standard images using Photoshop CC 2017 to reveal staining details of inverted images.

Results

Low power views of sagittal sections reveal staining patterns that are comparable between WT and CISD2 KO mice (Figure 1A and B). General staining features of oligodendrocytes (Figure 1C and D), and other cell types, was also similar between WT and CISD2 KO mice. Given these similarities, pictures from WT or CISD2 KO mice are used to depict subsequent examples of stained structures. Staining was present across all regions with staining widespread among many cell types, e.g., neurons, oligodendrocytes, myelin, choroid plexus, ependymal cells (Figures 2 and 3). At higher power, prominent densities of staining were observed
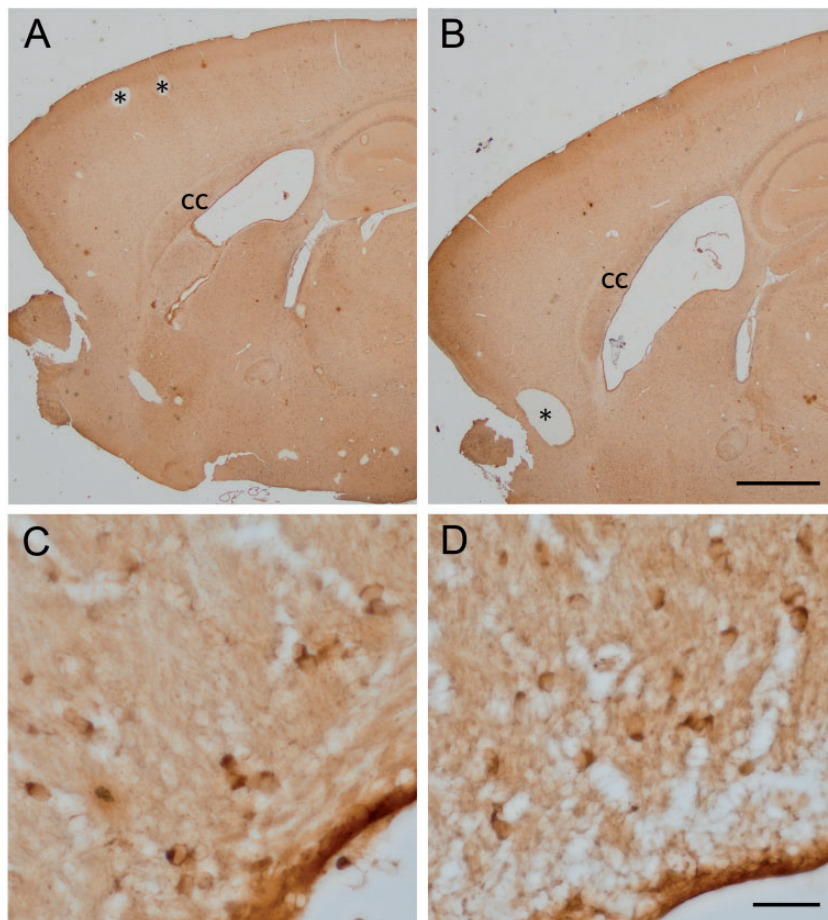

Figure 1. Low Power Sagittal Views of the Cerebrum Reveal Similar Patterns of Staining Between (A) WT and (B) CISD2 KO Mice. Areas devoid of staining (*) due to incomplete wetting of tissue. Corpus callosum (cc). Higher power views of the corpus callosum reveal oligodendrocytes with staining often concentrated to one side of the soma in both (C) WT and (D) CISD2 KO mice. Bar in B = 1 mm for panels A and B. Bar in D = 20 microns for panels C and D.
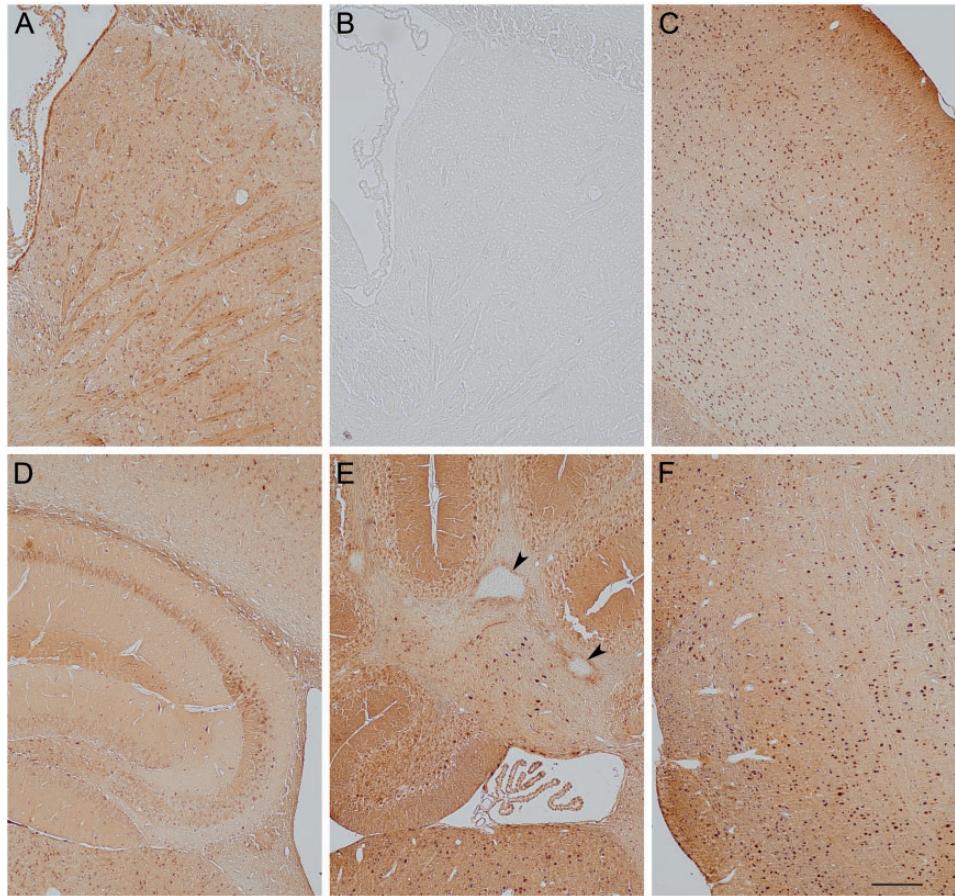
Figure 2. Cellular Staining Is Present in the (A) Caudate Putamen and Lateral Ventricle (B Is the Matching Control for A), (C) Cortex, (D) Hippocampus, (E) Cerebellum, and (F) Pons/Medulla. Note the staining of the choroid plexus (A, E), ependymal cells (A), neurons in the cortex (C) and hippocampus (D), and large neurons in the deep cerebellum (E) and pons/medulla (F). (B) A control solution, in place of the potassium ferrocyanide solution, did not result in staining. (E) Regions devoid of staining (arrowheads) were observed among stained areas. WT (A, B, D, E) and CISD2 KO (C, F) mice. Bar = 200 microns.

within the nucleus and cytoplasm (Figures 3 and 4). Staining was often present as discrete puncta (Figure 4). Although puncta were present within neurons of all sizes, they were particularly prominent, and easy to discern, within large neurons of the hindbrain (Figure 4). Typically, stained structures were distributed across the soma, but in some neurons, stained structures appeared to accumulate towards one side of the cell, e.g., towards the axon hillock (Figure 4D to F). Some stained structures within the cytoplasm appeared larger than others or aggregated (Figure 4G and H), which could be due to an actual size difference or that the structures were in close proximity and difficult to discern. Images that compressed information from multiple planes of focus, i.e., enhanced depth of focus, revealed that stained cytoplasmic structures were numerous (Figure 5). Staining within the nucleus was also discrete with the nucleolus and presumably chromatin features being prominent (Figure 5). Regions devoid of any staining, or with a rim of staining, were observed among stained areas in a random manner

that did not coincide with specific anatomical structures (Figures 1A, 1B, and 2E); these regions were attributed to incomplete wetting of these areas during the staining procedure due to the sharp demarcation, varying sizes, and varied distribution of the unstained areas. The use of acetone in the staining solution appeared to facilitate the wetting of tissue following the SafeClear step, and tapping the slides to remove excess SafeClear, before incubation in the staining solution, may reduce the degree of the unstained areas. In addition to unstained areas, there can be variability in the levels of staining between sections. Sections processed with the control solution revealed no staining (Figures 2B, 3B, 3B′, 4B, and 4I).

Since CNS tissue from autopsied human specimens underwent different processing than for mouse tissue (e.g., longer post-mortem interval), we performed an initial evaluation to determine if paraffin sections from human CNS tissue gave staining features similar to that observed for mouse CNS tissue. At low power, staining was observed across the sections in both white and gray
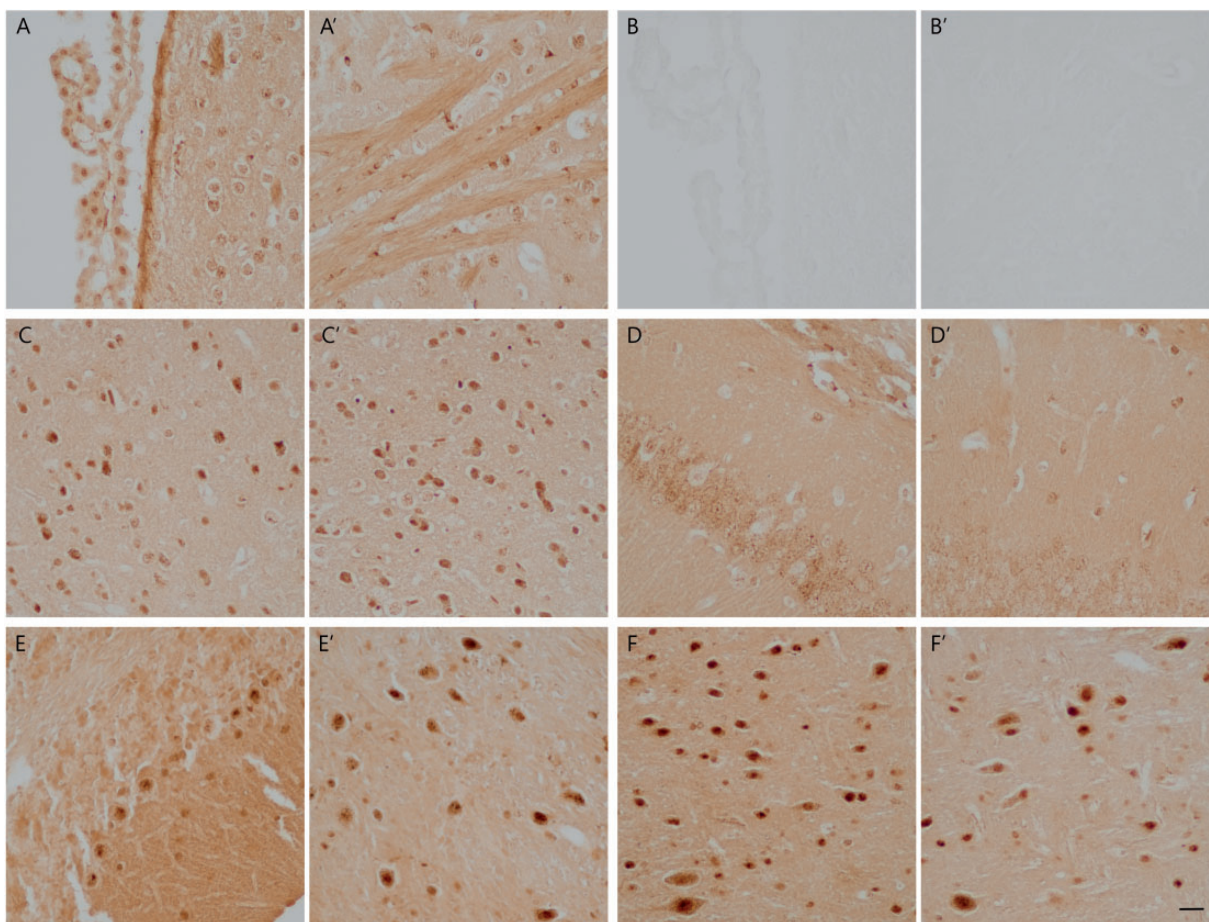
Figure 3. Higher Power Views of the Stained Areas Depicted in Figure 2. Note the staining of the choroid plexus and ependymal cells (A), myelin, oligodendrocytes and neurons in the caudate putamen (A'), neurons in the cortex (C, C'), neurons/neuronal layers stained in the hippocampus (D, D'), neurons in the layers of the cerebellum cortex (E), and large and smaller neurons in the deep cerebellum (E') and pons/medulla (F, F'). Neurons often displayed nuclear staining and cytoplasmic punctate staining. B, B') Incubation with a control solution, in place of the potassium ferrocyanide solution, revealed no staining. WT (A, A', B, B', D, D', E, E') and CISD2 KO (C, C', F, F') mice. Bar = 20 microns.

mater structures, but similar to mice there were also unstained areas (Figure 6), which appeared to be due to uneven wetting of the tissue by the staining solution. A preliminary examination of Alzheimer's disease tissue revealed light staining of some plaques containing more heavily labeled cellular processes and varied degrees of vascular staining (Figures 6 and 7). Vessels with iron deposits from Alzheimer's disease specimens had a range of diameters and were present within the parenchyma or meninges (Figures 6 and 7).

Neurons in both control and Alzheimer's disease tissue had various degrees of intracellular staining (Figure 8). Some neurons, particularly those in the hippocampus, had punctate staining in the cytoplasm and/or nucleus (Figure 8B, E, and F) while other neurons had staining that was less distinct and often appeared shrunken (Figure 8C), which is likely due to post-mortem changes and the retraction of the cell body following

immersion fixation (Koenig and Koenig, 1952; Garman, 1990). Staining was also present in oligodendrocytes (Figure 8G) and the choroid plexus (Figure 8H). In addition, some reactive astrocytes and reactive microglia were occasionally stained. The control solution revealed an absence of staining (Figure 8I).

Discussion

Previously, a modified iron histochemical procedure that was suitable for mouse paraffin CNS sections was described (Sands et al., 2016). Although this method had substantial improvements over other histochemical procedures to stain iron, the procedure incorporated some complex features and it had a high sensitivity that could often result in robust staining that obfuscated cellular staining details (Sands et al., 2016). Here we describe a simplified version of that procedure that
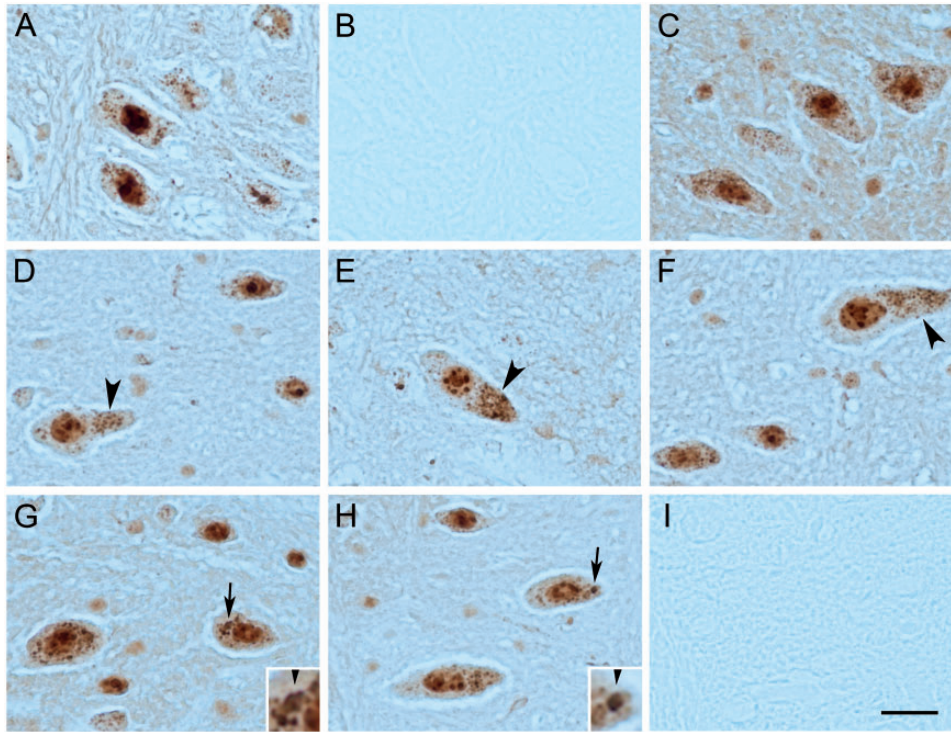
Figure 4. Examples of Large Stained Neurons in the Pons/Medulla from Wild Type (A, C) and CISD2 KO (D–H) Mice. Note prominent punctate staining within the nucleus and smaller punctate structures within the cytoplasm. In some cells (D–F) the cytoplasmic punctate structures were concentrated towards the axon hillock (arrowheads). In other neurons (G, H), some punctate structures appeared aggregated or larger than other cytoplasmic punctate structures (inset is a higher magnification of the site depicted at the arrow). Nuclear features often included staining of the nucleolus (e.g., circular structure at the center of the nucleus in E) and presumably chromatin (e.g., structures around the nucleolus in E). The nucleus also generally had an overall higher base level of staining than the cytoplasm. Slides from wild type (B) and CISD2 KO (I) mice revealed no staining when the control solution was used in place of the solution with potassium ferrocyanide. Bar = 20 microns (8 microns for the insets in G and H).

retains a key modification, i.e., direct staining following deparaffinization, and incorporates a key feature from another staining procedure (Hirose et al., 1970), i.e., utilization of acetone in the staining solution.

Direct staining after deparaffinization limits the extraction of iron that typically occurs following downgraded alcohol steps, which are normally used to hydrate sections. By limiting extraction, iron is detected in localizations that were not appreciated by other methods, e.g., neurons (Sands et al., 2016). A limitation of this method is that despite widespread staining, some areas of varying sizes may not get fully wetted and go unstained, but these regions are easily identified by microscopy. For instance, staining within one or more regions could abruptly cease and the unstained area could have a rounded appearance consistent with a residual drop of SafeClear, or residual paraffin, impeding the staining solution from accessing the tissue (e.g., Figures 1A and 6A to C). Removing excess SafeClear, via tapping of slides, may help reduce these unstained areas and acetone in the staining solution may help with wetting of tissue as slides incubated in staining solutions without acetone may have more or

larger unstained areas. The inclusion of acetone in the procedure was also found to increase the definition of stained structures by limiting the diffusion of the Prussian blue reaction product (Hirose et al., 1970). Thus, using a simplified procedure that both limits excess staining, which can obscure cellular structures, and incorporates acetone in the staining solution, results in greater definition of stained subcellular features.

With increased staining definition, investigations can be performed about the size, number and distribution of iron-rich subcellular structures in normal, developing and disease states. In neurons, particularly large neurons in the deep cerebellum and pons/medulla, cytoplasmic punctate structures were typically small (<1 micron) (e.g., Figure 5), often numerous (Figures 4 and 5), and widely dispersed within the cytoplasm. However, on occasion the punctate structures were observed to accumulate to one region of the soma, e.g., toward the axon hillock. It is unknown if during pathological conditions the cytoplasmic staining features become altered, and if so, to what extent. For example, in some instances the structures were aggregated and/or larger than others
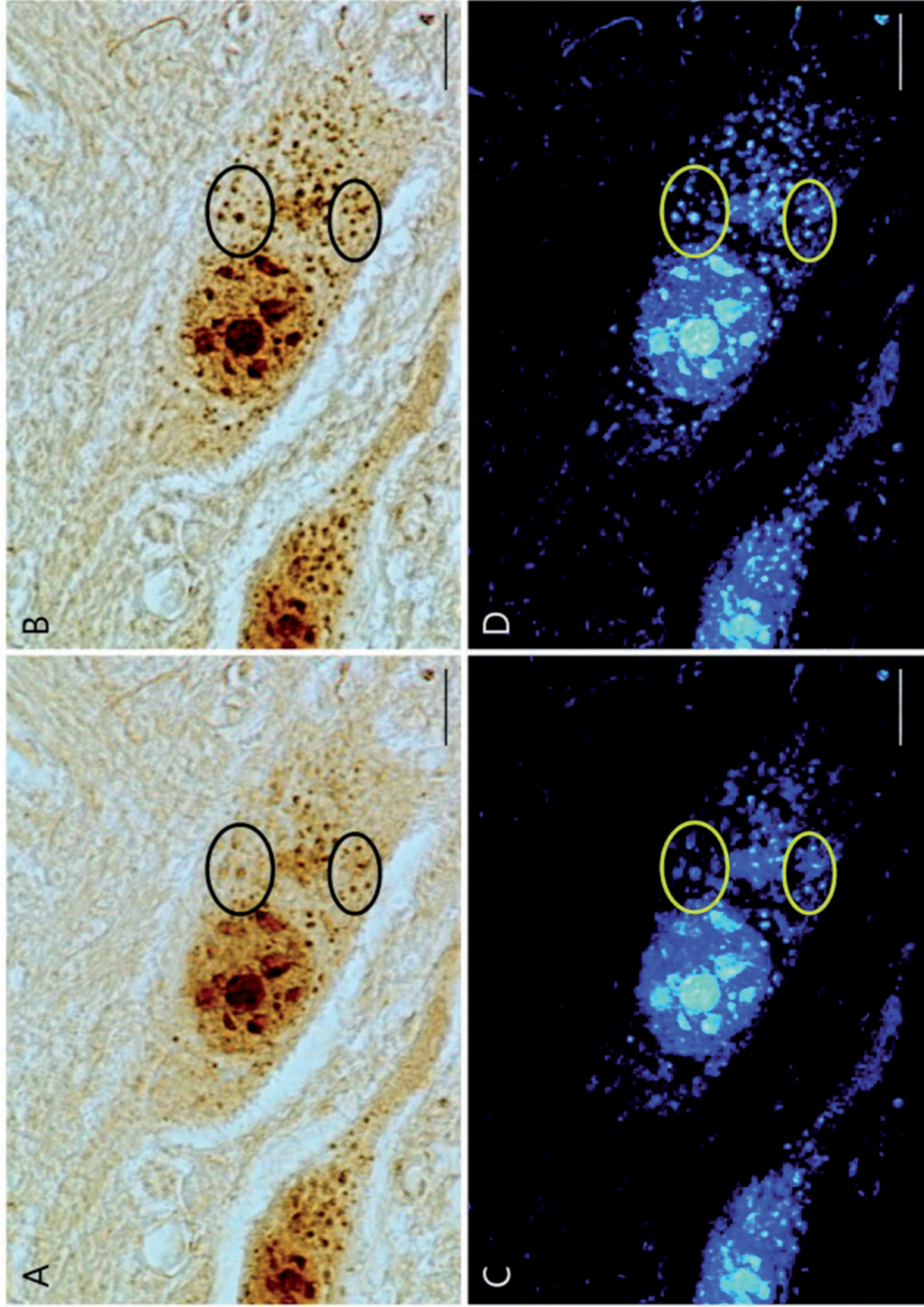
Figure 5. Discrete Staining Features Within Neurons. A single plane of focus image (A, C) and an extended depth of focus image (B, D) of large neurons in the pons/medulla shown as bright field images (A, B) and inverted images (C, D). Note, the number of punctate structures is substantially increased in the cytoplasm in the extended depth of focus image (B, D; e.g., black and yellow circles, respectively) compared to the single plane of focus image (A, C; e.g., black and yellow circles, respectively) indicating that these structures are separated from one another. In contrast, the number of punctate structures is not substantially increased in the nucleus in the extended depth of focus image compared to the image from a single plane of focus, although they are more clearly delineated in the former. The stained structures in the nucleus are also substantially larger than those in the cytoplasm. These stained nuclear features represent the nucleolus (largest circular structure within the center of the nucleus for the right cell) and presumably chromatin. The overall base level of staining of the nucleus is higher than that of the cytoplasm. Bars = 10 microns.
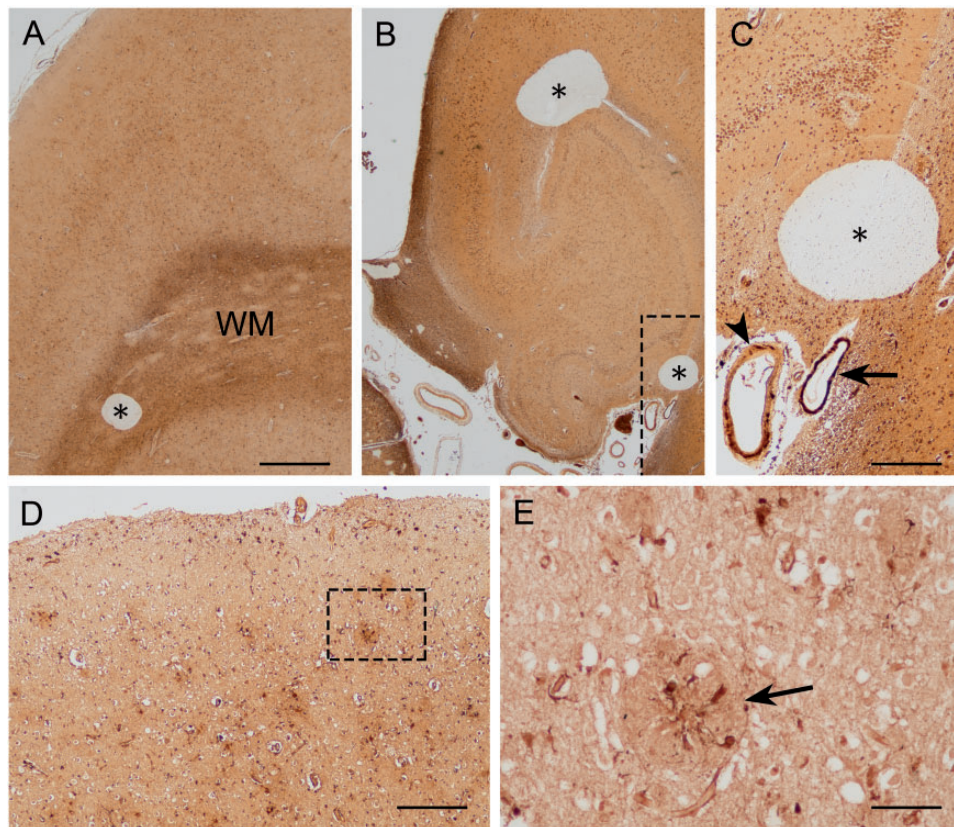
Figure 6. Stained Paraffin Sections From Autopsied Human Specimens of the Entorhinal Cortex/Hippocampus. At low power, staining is present in (A) white matter (WM) and overlying cortex (control subject), and (B) within the hippocampus (Alzheimer's disease subject). (C) A higher magnification of the region identified by the dashed lines in B reveals staining of neurons and varying degrees of staining within large vessels. The vessel at the arrow has extensive labeling around both its circumference and across its diameter while the vessel at the arrowhead has iron deposits that are distributed only partially around its circumference and partially across its diameter. The asterisks (*) in A-C represent unstained areas, which are thought to be due to incomplete wetting of tissue during the staining procedure. (D) A cortical region from a patient with Alzheimer's disease reveals neuronal staining and light staining of plaques. (E) A higher magnification of the boxed region in D reveals light plaque staining containing labeled processes (arrow). Control (A) and Alzheimer's disease (B-E) specimens. Bar in A = 1 mm for A and B. Bars in C and D = 250 microns. Bar in E = 50 microns.

cytoplasmic punctate structures (insets in Figure 4). Although these were observed in CISD2 KO mice, it is unknown if their size, number, and/or distribution are altered from control mice since a stereological analysis was beyond the scope of the present study that was focused on the development of the simplified staining procedure. Also, there might be cell loss in CISD2 mice, or in other neuropathological states, which could require normalization to determine whether there is an actual difference from control animals.

The leading candidates for the stained cytoplasmic structures are mitochondria and/or lysosomes. Mitochondria are sites of iron concentration, e.g., iron sulfur clusters, and they are a source of reactive oxygen species that can mediate cellular damage. Since CISD2 protein (CDGSH iron-sulfur domains 2) localizes to the outer mitochondrial membrane, and the endoplasmic reticulum (Wiley et al., 2013), it would not be unexpected if changes to stained cytoplasmic features were observed in CISD2 KO mice. Mutations in CISD2 are responsible for Wolfram Syndrome 2 in humans (Amr et al., 2007; Mozzillo et al., 2014), and these symptoms include early-onset diabetes, ataxia, hearing loss, and vision impairment (Urano, 2016). CISD2 KO mice not only recapture these phenotypes but also present nerve and muscle degeneration in association with mitochondrial damage, and autophagy-mediated cell death (Chen et al. 2009a; 2009b; Nobili et al., 2020). In addition, the lysosome is used in the cellular uptake of iron, and the lysosome and other structures associated with autophagy (e.g., auto-phagosome) are essential for the recycling of iron (Kurz et al., 2011). Therefore, the lysosome and/or autophagy-associated structures are also lead candidates accounting for the cytoplasmic punctate staining. Furthermore, CISD3, an isoform of CISD2, has been shown to regulate iron homeostasis (Lipper et al., 2018); thus, the role of CISD proteins in iron metabolism and disease states is an area of current interest.
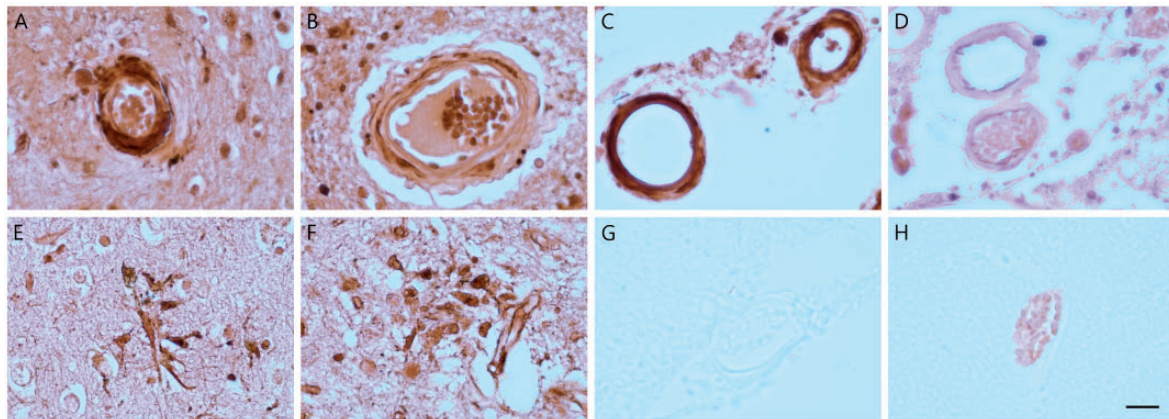
Figure 7. Vessels With Enhanced Deposition of Iron. In Alzheimer's disease, some vessels had varying degrees of enhanced deposition within the walls of vessels. The staining could be extensive throughout the entire width of the vessel wall (A, C) or within a portion of the vessel wall thickness (B). Stained vessels could be within the parenchyma (A, B) or meninges (C). In addition to larger vessels, some capillaries were stained, which could be seen in association with stained cells (E, F). Vessels from control subjects did not have evidence of extensive deposition of iron within vessels (D). Sections from Alzheimer's disease (G) or control (H) subjects incubated in a control solution generally revealed no or little staining, e.g., residual RBCs (H) or a very light brown hue in some neurons (not shown). Bar = 20 microns for A − H.
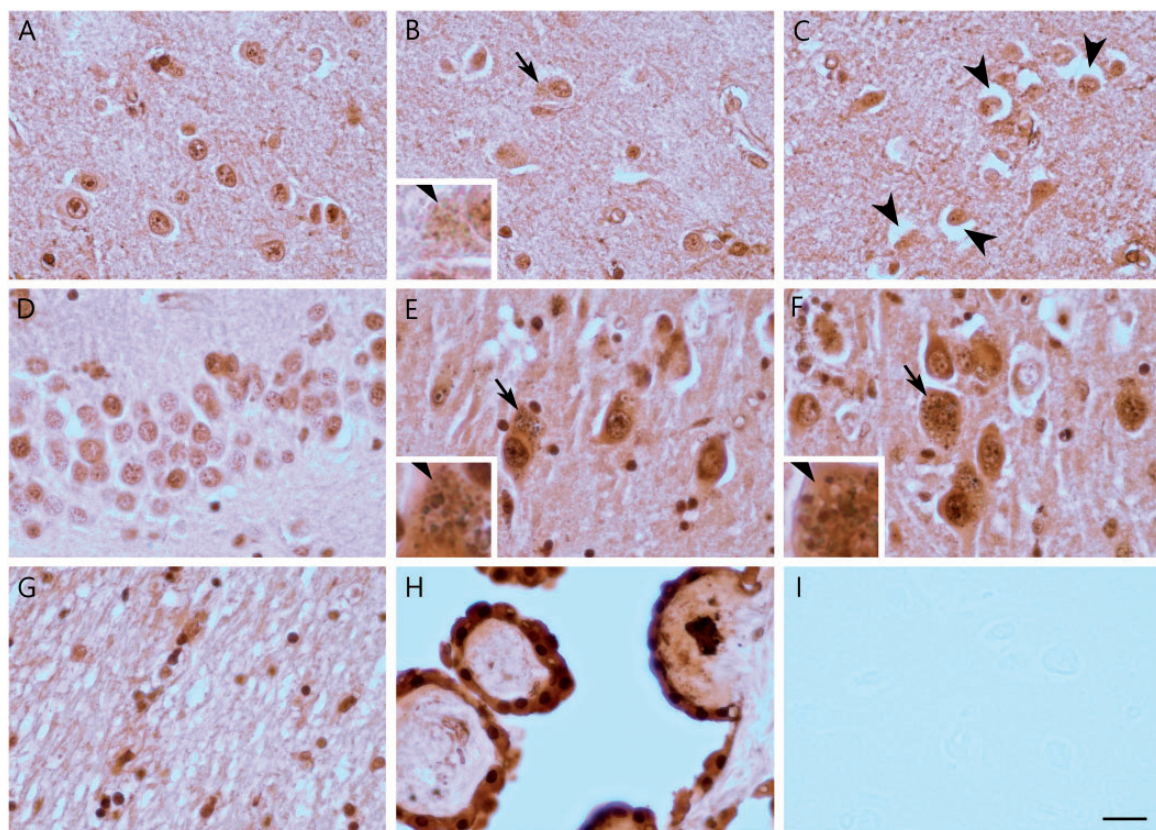

Figure 8. Neurons Revealed a Range of Staining Features: Prominent Nuclear Staining (A, B, D-F), Cytoplasmic Punctate Staining (B, E, F; also see inset which is a higher magnification of the areas depicted by the arrows) or Neurons With Less Distinct Features (B, C). Cytoplasmic punctate staining was more prominent within large neurons of the hippocampus (E, F). Shrinkage of neurons was also prevalent (e.g., arrowheads in C). In addition to neuronal staining, oligodendrocytes (G) and the choroid plexus (H) were stained. The control solution revealed an absence of staining (I). Tissue was from control (A–C, I) and Alzheimer's disease (D-H) cases. Bar = 20 microns for A–I (~6.7 microns for the insets for B, E, F).

Besides neuronal staining, other cell types, such as ependymal cells, the choroid plexus, and oligodendrocytes, were labeled. Previous studies also found that iron was enriched within ependymal cells (Erb et al., 1996) and the choroid plexus, with the latter study obtaining data suggesting that iron accumulates in lysosomes (da Cruz Fernandes et al., 2018). Histochemical studies have also detected the concentration of iron within oligodendrocytes (Hill and Switzer, 1984; Gerber and Connor, 1989; LeVine and Macklin, 1990; LeVine, 1991; Connor and Menzies, 1995), and the high density of iron within these cells was further substantiated by particle-induced X-ray emission microscopy (Reinert et al., 2019). Interestingly, that study also found that within rat neurons, iron was most concentrated in the nucleolus, followed by the nucleus and then the cytoplasm, but since the cytoplasm was the largest compartment it accounted for $73 \pm 17\%$ of the neuronal iron (Reinert et al., 2019). Also, within the cytoplasm of neurons, iron was found to be concentrated in small spots, which was similar to the findings in the present study, but their results indicated that microsomal fraction (consisting of endoplasmic reticulum, ribosomes, vesicles, plasma membrane), and not mitochondria or lysosomes, accounted for the majority of iron (Reinert et al., 2019).

The simplified method described here was also used to perform an initial study of human CNS tissue. We show that some neurons in the human entorhinal cortex/hippocampus have both discrete staining within the nucleus and punctate staining of cytoplasmic structures. However, other neurons were devoid of distinct staining features and appeared shrunken. It is likely that the longer postmortem interval for human specimens compared to mouse specimens affected the morphology of the neurons as well as the stainability of distinct subcellular structures. In addition, an extended duration of fixation could affect the ability to detect iron by histochemistry (Connor and Menzies, 1995). Besides neuronal staining, oligodendrocytes and the choroid plexus were stained.

In Alzheimer's disease specimens, extensive deposition of iron could be observed associated with some vessels with this methodology, but it is unknown how common this finding is among patients with this disease. Staining of larger vessels was more readily apparent in one of the two cases. Since the patients were also determined to have cerebral amyloid angiopathy, it is possible that the vascular iron deposition was associated with the amyloid (Bulk et al., 2018b). However, widespread staining of plaques was not revealed by the present preliminary investigation, which would argue against this association accounting for vessel staining. The limited staining of plaques is in contrast to the findings from the more extensive method used on paraffin sections from APP/PS1 mice that revealed robust staining of plaques (Sands et al., 2016), which raises the possibility that acetone in this new method is limiting the detection of iron within plaques. Since these patients also had atherosclerosis, this comorbidity could be another factor influencing the deposition of iron in vessels. Occasionally, other pathological features, e.g., some areas of astrocyte gliosis and reactive microglia, were also revealed by this staining method.

In summary, we put forward a simplified method that detects iron within paraffin sections of CNS tissue. This method allows for the discrete staining of subcellular structures of neurons as well as revealing the accumulation of iron within other cell types. It is intended that this histochemical procedure will be employed to help advance the characterization and understanding about the pathogenic role of iron in various disease states of the nervous system.

Declaration of Conflicting Interests

Funding

ORCID iDs

Steven M. LeVine (ID) https://orcid.org/0000-0003-1623-148X
Sarah E. Tague (ID) https://orcid.org/0000-0001-9637-5701

References

Adams, C. W. (1988). Perivascular iron deposition and other vascular damage in multiple sclerosis. *J Neurol Neurosurg Psychiatry*, 51(2), 260–265.

Amr, S., Heisey, C., Zhang, M., Xia, X. J., Shows, K. H., Ajlouni, K., Pandya, A., Satin, L. S., El-Shanti, H., & Shiang, R. (2007). A homozygous mutation in a novel

zinc-finger protein, ERIS, is responsible for Wolfram syndrome 2. *Am J Human Genet*, *81*(4), 673–683.

Bulk, M., Abdelmoula, W. M., Nabuurs, R. J. A., van der Graaf, L. M., Mulders, C. W. H., Mulder, A. A., Jost, C. R., Koster, A. J., van Buchem, M. A., Natté, R., Dijkstra, J., & van der Weerd, L. (2018a). Postmortem MRI and histology demonstrate differential iron accumulation and cortical myelin organization in early- and late-onset Alzheimer's disease. *Neurobiol Aging*, *62*, 231–242.

Bulk, M., Moursel, L. G., van der Graaf, L. M., van Veluw, S. J., Greenberg, S. M., van Duinen, S. G., van Buchem, M. A., van Rooden, S., & van der Weerd, L. (2018b). Cerebral amyloid angiopathy with vascular iron accumulation and calcification. *Stroke*, *49*(9), 2081–2087.

Castelnau, P. A., Garrett, R. S., Palinski, W., Witztum, J. L., Campbell, I. L., & Powell, H. C. (1998). Abnormal iron deposition associated with lipid peroxidation in transgenic mice expressing interleukin-6 in the brain. *J Neuropathol Exp Neurol*, *57*(3), 268–282.

Chen, Y. F., Kao, C. H., Chen, Y. T., Wang, C. H., Wu, C. Y., Tsai, C. Y., Liu, F. C., Yang, C. W., Wei, Y. H., Hsu, M. T., Tsai, S. F., & Tsai, T. F. (2009a). Cisd2 deficiency drives premature aging and causes mitochondria-mediated defects in mice. *Genes Dev*, *23*(10), 1183–1194.

Chen, Y. F., Kao, C. H., Kirby, R., & Tsai, T. F. (2009b). Cisd2 mediates mitochondrial integrity and life span in mammals. *Autophagy*, *5*(7), 1043–1045.

Connor, J. R., & Menzies, S. L. (1995). Cellular management of iron in the brain. *J Neurol Sci*, *134*(Suppl), 33–44.

Connor, J. R., Menzies, S. L., St Martin, S. M., & Mufson, E. J. (1990). Cellular distribution of transferrin, ferritin, and iron in normal and aged human brains. *J Neurosci Res*, *27*(4), 595–611.

Craelius, W., Migdal, M. W., Luessenhop, C. P., Sugar, A., & Mihalakis, I. (1982). Iron deposits surrounding multiple sclerosis plaques. *Arch Pathol Lab Med*, *106*(8), 397–399.

da Cruz Fernandes, M., Severino, A. G., Zago, A. M., Tortorelli, L., Carvalho, F. B., & Schneider, F. L. (2018). Iron localization in the guinea pig choroid plexus: A light and transmission electron microscopy study. *J Trace Elem Med Biol*, *49*, 128–133.

Dong, X. H., Gao, W. J., Kong, W. N., Xie, H. L., Peng, Y., Shao, T. M., Yu, W. G., & Chai, X. Q. (2015). Neuroprotective effect of the active components of three Chinese herbs on brain iron load in a mouse model of Alzheimer's disease. *Exp Therap Med*, *9*(4), 1319–1327.

Erb, G. L., Osterbur, D. L., & LeVine, S. M. (1996). The distribution of iron in the brain: Aphylogenetic analysis using iron histochemistry. *Brain Res Dev Brain Res*, *93*(1-2), 120–128.

Garman, R. H. (1990). Artifacts in routinely immersion fixed nervous tissue. *Toxicol Pathol*, *18*(1 Pt 2), 149–153.

Gerber, M. R., & Connor, J. R. (1989). Do oligodendrocytes mediate iron regulation in the human brain? *Ann Neurol*, *26*(1), 95–98.

Hill, J. M., & Switzer, R. C. III. (1984). The regional distribution and cellular localization of iron in the rat brain. *Neuroscience*, *11*(3), 595–603.

Hirose, S., Yasutomi, M., Murai, N., Yamada, R., Katayama, A., Tsujino, M., Iwasa, Z., & Razzaq, A. K. A. (1970). A modified method of the Prussian blue reaction for the histochemical demonstration of iron, and its application to the colloidal iron reaction of acid mucopolysaccharides. *Acta Histochem Cytochem*, *3*(1), 18–27.

Koenig, R. S., & Koenig, H. (1952). An experimental study of post mortem alterations in neurons of the central nervous system. *J Neuropathol Exp Neurol*, *11*(1), 69–78.

Kontoghiorghes, G. J., Goddard, J. G., Bartlett, A. N., & Sheppard, L. (1990). Pharmacokinetic studies in humans with the oral iron chelator 1,2-dimethyl-3-hydroxypyrid-4-one. *Clin Pharmacol Therap*, *48*(3), 255–261.

Kurz, T., Eaton, J. W., & Brunk, U. T. (2011). The role of lysosomes in iron metabolism and recycling. *Int J Biochem Cell Biol*, *43*(12), 1686–1697.

LeVine, S. M., & Macklin, W. B. (1990). Iron-enriched oligodendrocytes: A reexamination of their spatial distribution. *J Neurosci Res*, *26*(4), 508–512.

LeVine, S. M. (1991). Oligodendrocytes and myelin sheaths in normal, quaking and shiverer brains are enriched in iron. *J Neurosci Res*, *29*(3), 413–419.

Lipper, C. H., Karmi, O., Sohn, Y. S., Darash-Yahana, M., Lammert, H., Song, L., Liu, A., Mittler, R., Nechushtai, R., Onuchic, J. N., & Jennings, P. A. (2018). Structure of the human monomeric NEET protein MiNT and its role in regulating iron and reactive oxygen species in cancer cells. *Proc Natl Acad Sci USA*, *115*(2), 272–277.

Moos, T., & Morgan, E. H. (2002). A morphological study of the developmentally regulated transport of iron into the brain. *Dev Neurosci*, *24*(2-3), 99–105.

Mozzillo, E., Delvecchio, M., Carella, M., Grandone, E., Palumbo, P., Salina, A., Aloi, C., Buono, P., Izzo, A., D'Annunzio, G., Vecchione, G., Orrico, A., Genesio, R., Simonelli, F., & Franzese, A. (2014). A novel CISD2 intragenic deletion, optic neuropathy and platelet aggregation defect in Wolfram syndrome type 2. *BMC Med Genet*, *15*, 88.

Nobili, A., Krashia, P., & D'Amelio, M. (2020). Cisd2: a promising new target in Alzheimer's disease†. *J Pathol*, *251*(2), 113–116.

Reinert, A., Morawski, M., Seeger, J., Arendt, T., & Reinert, T. (2019). Iron concentrations in neurons and glial cells with estimates on ferritin concentrations. *BMC Neuroscience*, *20*(1), 25.

Sands, S. A., Leung-Toung, R., Wang, Y., Connelly, J., & LeVine, S. M. (2016). Enhanced histochemical detection of iron in paraffin sections of mouse central nervous system tissue: Application in the APP/PS1 mouse model of Alzheimer's disease. *ASN Neuro*, *8*(5), 1759091416670978.

Urano, F. (2016). Wolfram syndrome: Diagnosis, management, and treatment. *Curr Diabetes Rep*, *16*(1), 6.

Walton, J. C., & Kaufmann, J. C. (1984). Iron deposits and multiple sclerosis. *Arch Pathol Lab Med*, *108*(9), 755–756.

Wiley, S. E., Andreyev, A. Y., Divakaruni, A. S., Karisch, R., Perkins, G., Wall, E. A., van der Geer, P., Chen, Y. F., Tsai, T. F., Simon, M. I., Neel, B. G., Dixon, J. E., & Murphy, A. N. (2013). Wolfram syndrome protein, Miner1, regulates sulphydryl redox status, the unfolded protein response, and Ca2+ homeostasis. *EMBO Mol Med*, *5*(6), 904–918.